

Sampling possible reconstructions of undersampled acquisitions in MR imaging

Kerem C. Tezcan, Christian F. Baumgartner and Ender Konukoglu^{*†}

June 8, 2022

Abstract

Undersampling the k-space during MR acquisitions saves time, however results in an ill-posed inversion problem, leading to an infinite set of images as possible solutions. Traditionally, this is tackled as a reconstruction problem by searching for a single "best" image out of this solution set according to some chosen regularization or prior. This approach, however, misses the possibility of other solutions and hence ignores the uncertainty in the inversion process. In this paper, we propose a method that instead returns multiple images which are possible under the acquisition model and the chosen prior. To this end, we introduce a low dimensional latent space and model the posterior distribution of the latent vectors given the acquisition data in k-space, from which we can sample in the latent space and obtain the corresponding images. We use a variational autoencoder for the latent model and the Metropolis adjusted Langevin algorithm for the sampling. This approach allows us to obtain multiple possible images and capture the uncertainty in the inversion process under the used prior. We evaluate our method on images from the Human Connectome Project dataset as well as in-house measured multi-coil images and compare to two different methods. The results indicate that the proposed method is capable of producing images that match the ground truth in regions where acquired k-space data is informative and construct different possible reconstructions, which show realistic structural variations, in regions where acquired k-space data is not informative.

Keywords: Magnetic Resonance image reconstruction, uncertainty estimation, inverse problems, sampling, MCMC, deep learning, unsupervised learning.

1 Introduction

Undersampling the k-space in MR imaging reduces scan time by speeding up acquisition, allowing a higher throughput as well as higher comfort for patients. However, contrary to a fully acquired k-space, where an inverse Fourier transform is mostly enough to uniquely determine the underlying image up to measurement noise, the undersampled acquisition leads to an underdetermined system of equations. Mathematically, this means that there are infinitely many images that match the acquired portion of the k-space data and it is impossible to know which one is the underlying image in a general setting.

Traditionally, this problem of infinitely many solutions has been tackled as a deterministic reconstruction problem, where different methods were proposed to choose a single "best" image out of the set of possible images. This was achieved by introducing some prior information in addition to the data consistency term through defining a regularization term that implicitly prefers a solution according to its certain properties, such as smoothness with Tikhonov regularization [1], sparsity of its gradients with total variation regularization [2] or how well it matches with some lower resolution version of the image [3]. This converts the problem into a well-posed regularized inverse problem and allows to obtain a single solution as the reconstructed image. Another way of seeing this approach is from the Bayesian framework, where the data consistency and regularization terms correspond to the data likelihood and prior terms, respectively. Here, again, a suitable prior along with the data likelihood allows to write the corresponding posterior probability which then can be maximized to obtain the maximum-a-posteriori (MAP) image as the single "best" reconstruction [4].

By providing a single reconstructed image as their output, these approaches miss the uncertainty in the solution that arises due to the missing portion of the k-space data. The reconstructed image is formed using information from the measured data and the

^{*}This work was supported by the Swiss National Science Foundation under Grant 205321.173016.

[†]All authors are with the Computer Vision Lab, ETH Zurich, Switzerland. Emails are {tezcan, baumgartner, kender}@vision.ee.ethz.ch

prior. Measured data matches the underlying true image up to the measurement noise while the prior complements the unmeasured information. However, it is important to remember that the prior is independent of the underlying true image and hence, the image that best satisfies the prior need not be the same as the true image. There is an inherent ambiguity. When a single reconstructed image is output, information coming from the prior is treated as definite. This treatment implicitly sacrifices the opportunity to reveal the inherent ambiguity in the reconstructed image.

An alternative approach, which we will pursue in this work is producing multiple images as solutions to the ill-posed inverse problem, where the images match the measured data while being highly likely according to the prior at the same time. Such an approach is capable of capturing the uncertainty in the inversion due to the missing data. The idea is that in this case the information from the prior is not treated as definite, but rather possibility of different images is explored under the specific prior used.

As the proposed approach provides multiple images, clinical, research or further analysis tasks, such as segmentation, can be applied separately on each image to propagate the uncertainty to any given task’s output. Alternatively the uncertainty can be quantified at the image level and passed on the following tasks, such as in the form of a mean image along with a standard deviation map. Inspecting the images or the quantified uncertainty for different regions can also be indicative of which parts of the images might be more prone to differ from the underlying true image. To the best of our knowledge, this is the first time such an approach is being proposed for undersampled MRI acquisition.

In the recent years, though not directly related to the uncertainty due to missing data in undersampled MRI, there has been research efforts to quantify uncertainty in different aspects of the image reconstruction problem, especially with the deep learning based models [5]. One such aspect is the *epistemic* or model uncertainty, i.e. the uncertainty in the mapping learned by the neural network used in the reconstruction, which can be obtained using approaches such as drop-out [6]. However, these approaches quantify the uncertainty due to the ambiguity in the network parameters and do not capture the uncertainty due to the missing k-space data. Epistemic uncertainty tends to zero as the training set size goes to infinity [7], however, increasing training samples cannot be expected to diminish the ambiguity due to missing k-space data. Another aspect is the so called *aleatoric* uncertainty due to noise or other

ambiguities in the images or the labels, which is more relevant to reconstruction from undersampled MRI. Quantifying aleatoric uncertainty can be approached using, for instance, heteroscedastic models. These models predict a different variance value for each output pixel and hence can in principle learn to predict high variance for pixels where the model expects to have incorrect mean predictions. There is one important limitation to these models. They generate only second order statistics of pixel-wise marginal distributions. Such a model may be useful in predicting pixels where predictions may be inaccurate, however, it cannot propose different possible reconstructions. For this, non-Gaussian pixel-wise distributions and non-trivial statistical dependencies across different pixels are crucial to capture. Hence these models are limited in the information they can provide [8]. Being able to generate samples makes uncertainty propagation trivial for any following task while only generating second order statistics makes this non-trivial.

One work that has similar aims as this paper is by Adler et al. [9]. In this work, the authors train a modified conditional Wasserstein generative adversarial network (cWGAN) that generates high dose counterparts of CT images from low-dose measurements. However this approach does not explicitly model the known physics or the measurement noise of the imaging procedure, lacking an explicit data likelihood term. As such, there are no guarantees that the samples will be from the true posterior. Instead of using an explicit physics-based imaging model, the cWGAN requires supervised training with pairs of undersampled-fully sampled images, hence a separate cWGAN has to be trained for all different undersampling schemes and factors for best performance. Furthermore, though the authors modify their discriminator to reduce the mode collapse associated with the WGAN, they do not completely avoid it, leading to a possibly poorer implicit prior. Lastly, the model aims to minimize the Wasserstein distance between the predicted posterior and the true posterior. However, it is often impossible to have varying samples from the true posterior, in reality only one fully measured image is available for each low-dose measurement image. Therefore, the available training samples may not be able to support an accurate posterior approximation and minimizing the Wasserstein distance may converge to a degenerate version of the true posterior.

Another work in line with our purposes is by Pedemonte et al. [10], where the authors use Hamiltonian Monte Carlo (HMC) to sample from the posterior of emission rates given the photon counts for positron emission tomography. However, they use a uniform,

i.e. a non-informative prior for the emission rates, reducing the strength of the model heavily in contrast to using more informative, data-driven priors. Furthermore the authors use a Riemannian HMC scheme [11] to make sampling efficient despite the high dimensional posterior, where the use of the Riemannian metric speeds up the sampling by taking the geometry of the space of probability distributions into account. However this does not directly take into account the geometry of the space of the emission rates.

Here we identify two ideas that motivate us in proposing a new method that overcomes the limitations of the works mentioned above. The first one is regarding the geometry of the space of MR images. We make the assumption that the MR images actually live around a low dimensional subspace in the high dimensional image space and that we can learn a mapping from a low dimensional latent space to this subspace. This assumption has been demonstrated empirically in our prior work [4]. Then "walking around" and sampling in the subspace of MR images can be simply implemented as walking around and taking samples in the latent space. Secondly, deep learning based data-driven priors have shown great value in inverse problems in general in the recent years, as well as specifically in MR image reconstruction [4,12,13]. Such methodology allows learning a powerful mapping between the latent space and the image space, facilitating the sampling.

Embodying the ideas mentioned above, we propose a novel method based on a latent Bayesian model and Markov chain Monte Carlo (MCMC) sampling that addresses the issue of uncertainty in the inversion process. To this end, we use a variational autoencoder (VAE) [14,15] trained on fully sampled MR images as our prior and utilize its lower dimensional latent space to do the sampling instead of sampling in the high dimensional image space. For the target distribution of the MCMC, we use the posterior of the latent vectors given the measured k-space data. We obtain this distribution by marginalizing over the images. We use the Metropolis adjusted Langevin Algorithm (MALA) [11] as the MCMC method due to its effectiveness in high dimensional spaces. The latent samples coming from MALA are then guaranteed to be from the posterior and can be transformed to images using the decoder of the VAE. Although we use a VAE and MALA in our implementation, the framework is generic and can be used with other generative models as well as sampling schemes. We evaluate our method with data from the Human Connectome Project (HCP) [16] as well as in-house measured images [4] for changing settings of undersampling ratios and measurement noise levels and compare it to two

other methods.

2 Methods

We are interested in obtaining samples from the posterior distribution $p(x|y)$ of images $x \in \mathcal{C}^N$ given the observed undersampled noisy k-space data $y \in \mathcal{C}^{Mc}$ with c coils, ($M \leq N$). We model the acquisition as $y = Ex + \eta$, where $E \in \mathcal{C}^{Mc \times N}$ is the extended MR encoding operation and η is complex Gaussian noise in the k-space with $\eta \sim N(0, \Sigma_{ns})$ with Σ_{ns} as the noise covariance matrix. Hence the data likelihood term is given as $p(y|x) = N(y; Ex, \sigma_{ns})$. The extended encoding operation comprises of the usual coil sensitivity encoding [17], Fourier transform and undersampling operations, and additionally of a scaling factor, a padding operator, an operation for combining the phase with the magnitude image and an operator for modeling the bias field [18,19] in the image, which we explain further in Section 2.5.

Unfortunately, it is difficult to draw samples directly from their posterior $p(x|y)$ since the x 's are very high dimensional. This renders simple sampling methods such as rejection sampling or vanilla MCMC [20] very inefficient since they would need too many samples to adequately travel around in the space to generate a good representation of the posterior. Moreover, the assumption that the high probability regions in the image space form a lower dimensional subspace would drastically lower the acceptance ratio for the samples. For instance, if the sampling is done in the image space using MCMC, the random walk will try to move in dimensions that will take it out of this lower dimensional subspace and sampling will become very inefficient. On the other hand, if we have a latent space connected to the lower dimensional subspace with a decoder, then we can implement the random walk in the latent space, and the images decoded from the latent samples will always be around this lower dimensional subspace.

The proposed model here samples directly in the lower dimensional latent space to address the difficulties mentioned above. To this end we use a VAE as the latent space model. This allows us to first sample latent vectors and then use the decoder of the VAE to obtain images from these.

In the following we describe the method in more detail.

2.1 Sampling in the latent space

Firstly, we need a prior term for the MR images with which we can evaluate the probability of a given image and also differentiate. To this end, we

use a VAE [14, 15] trained on fully sampled MR images. The trained VAE consists of an encoder $q(z|x) = N(\mu_z(x), \Sigma_z(x))$ and a decoder $p(x|z) = N(\mu_x(z), \Sigma_x)$ parameterized by neural networks with $z \in \mathcal{R}^D$ ($D < N$) as latent vectors distributed according to a Gaussian prior $p(z) = N(\mu_{pr}, \Sigma_{pr})$. We drop the x and z dependencies in the rest of the text unless necessary. Here we use a diagonal non-isotropic covariance matrix for Σ_z , an isotropic diagonal matrix for Σ_x and a block diagonal for the Σ_{pr} . The VAE is trained to maximize the evidence lower bound (ELBO) which approximates the log likelihood $p(x)$. For the prior $p(z)$, we empirically estimate the parameters μ_{pr} and Σ_{pr} from training data [21], which is different than the case in the vanilla VAE, which we explain in Section 2.4.

Now, given the VAE, we can formalize our aim as to sample from the posterior of latent variables given the undersampled k-space data, namely $p(z|y)$. By doing so we obtain latent samples that match the measured k-space data and thus, the images associated with these latent samples will match the data too. However, before we describe how we obtain this distribution, we first introduce the sampling procedure.

Sampling from $p(z|y)$ can be implemented using different methods. In this work, we use the Metropolis adjusted Langevin algorithm (MALA) [11]. MALA is a variant of Markov chain Monte Carlo, consisting of a random walk given by Langevin dynamics and an acceptance scheme following the Metropolis-Hastings algorithm. The random walk for MALA with the target distribution $p(z|y)$ is written as

$$\hat{z}^{t+1} = z^t + \tau \nabla_z \log p(z|y)|_{z=z^t} + \sqrt{2\tau} \zeta, \quad \zeta \sim N(0, 1) \quad (1)$$

with step size τ . As can be observed, the update step for the random walk is composed of two terms. The second term models the randomness with a Gaussian distributed variable ζ , aiming to discover the space equally in all directions. As the latent space can be large, only sampling with the random part can be inefficient for sampling from $p(z|y)$. Here, the first term $\tau \nabla_z \log p(z|y)$ comes to aid by pulling the steps towards the high probability regions and preventing the random walk to move far away from such regions. However, the discrete nature of the walk requires a Metropolis-Hastings correction to be applied to ensure convergence. This means a sample is accepted as $z^{t+1} = \hat{z}^{t+1}$ with log probability $\alpha = \min \left\{ 0, \log \left[\frac{p(\hat{z}^{t+1}|y)q(z^t|\hat{z}^{t+1})}{p(z^t|y)q(\hat{z}^{t+1}|z^t)} \right] \right\}$, otherwise $z^{t+1} = z^t$. The proposal distribution for MALA is given as $q(z'|z) \propto \exp \left(-\frac{1}{4\tau} \|z' - z - \tau \nabla \log p(z|y)\|_2^2 \right)$. Further-

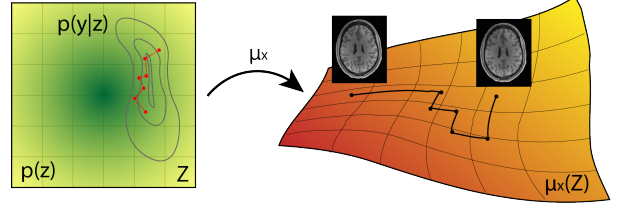


Figure 1: Illustration of sampling in the latent space. Left side shows the latent space equipped with a prior shown by the green color. The contours show the regions where z values result in high data likelihood values for the measured data. The random walk (red line) samples from the product of these two, i.e. the posterior $z^t \sim p(z|y) \propto (y|z)p(z)$. Right side shows the low dimensional subspace around which the MR images reside. Each sample in the Z space correspond to a distribution of images in the subspace, s.t. an image can be taken using the the mean of decoder of the VAE as $x^t = \mu_x(z^t)$.

more, in order to avoid a long burn-in period, we can initialize the chain close to the mode of the posterior instead of starting with a randomly chosen z^0 . This can be achieved by encoding the MAP image into the latent space and using its mean as z^0 .

Once the posterior samples $\{z^t\}$ are obtained, we then take samples from the posterior of the images as $x^t = \mu^t$, i.e. the mean of the decoder $p(x|z)$ when $z = z^t$. Notice that this procedure is quite similar to ancestral sampling due to the hierarchical structure of the model, however, without the sampling step on the image level. Now these image samples can be passed on to further tasks or used to calculate empirical statistics such as pixel-wise mean and variance.

2.2 Obtaining the posterior $p(z|y)$

The main component required for the random walk is the unnormalized posterior distribution of z , i.e. $p(y|z)p(z) \propto p(z|y)$, where we do not need the normalization constant $p(y)$ since it does not appear in the derivative nor the acceptance terms. To construct it, we use the trained VAE model with its prior $p(z) = N(\mu_{pr}, \Sigma_{pr})$. We write the $p(y|z)$ term as a marginalization over the images as

$$p(y|z) = \int p(y, x|z) dx = \int p(y|x)p(x|z) dx, \quad (2)$$

where we use the decoder of the VAE as the $p(x|z)$ and the conditional independence assumption $p(y|x, z) = p(y|x)$. This expression can be interpreted as two terms glued together with the images functioning as the intermediate variables, connecting the

latent space with the k-space. This integral can be evaluated analytically to yield another Gaussian distribution [22]. After isolating the terms constant with z and taking the logarithm, this distribution is given as

$$\begin{aligned} \log p(y|z) = & \mu_x^H \Sigma_x^{-1} (\Sigma_x^{-1} + E^H \Sigma_{ns}^{-1} E)^{-1} \Sigma_x^{-1} \mu_x \\ & + 2\text{Re} \{ y^H \Sigma_{ns}^{-1} E (\Sigma_x^{-1} + E^H \Sigma_{ns}^{-1} E)^{-1} \Sigma_x^{-1} \mu_x \} \\ & - \frac{1}{2} \mu_x^H \Sigma_x^{-1} \mu_x + C. \end{aligned} \quad (3)$$

where H denotes the conjugate transpose and C is some constant w.r.t. z . We provide the details of this derivation in the Appendix due to space restrictions.

For the random walk we also need the log gradient of the target distribution, which we write as $\nabla_z \log p(z|y) = \nabla_z \log p(y|z) + \nabla_z \log p(z)$. The $\nabla_z \log p(y|z)$ term can be easily obtained by automatic differentiation since outputs of the decoder μ_x and Σ_x are modeled as neural networks and, thus, differentiable w.r.t z , given that we can implement $p(y|z)$ in a software package that allows such differentiation. Similarly, the prior $\nabla_z \log p(z)$ term is also straightforward and can be derived analytically. The more challenging part is the matrix inversion $(\Sigma_x^{-1} + E^H \Sigma_{ns}^{-1} E)^{-1}$ in Eq. 3, which we investigate in the next section.

Finally, looking at the two terms in the posterior $p(z|y) \propto p(y|z)p(z)$ reveals more insights regarding the method. The first term drives the chain to regions where the z^t values, when decoded as $p(x|z^t)$, lead to images which satisfy the data likelihood term $p(y|x)$ for x 's coming from the $p(x|z^t)$. On the other hand, the second term $p(z)$ tries to pull the chain towards the middle of the empirical Gaussian in the latent space, discouraging the chain to move away from the meaningful regions of the latent space. As such, a random walk in the latent space with this target distribution explores the areas which satisfy the data likelihood and the prior terms simultaneously.

One natural alternative to the proposed method is to use the approximation posterior $q(z|x)$ modeled in VAE directly to do the sampling around a MAP estimate x_{MAP} , i.e. taking latent samples around the conditional distribution $z^t \sim q(z|x_{MAP})$ and then again decoding these to the image space. This approach is fundamentally different than the proposed method in that it takes the MAP image as the "true reconstruction" and samples only locally around it. Though these locally sampled images will still be in the subspace of MR images and show some structural variation, they do not explore the possibility of different images being the true underlying image. Hence

the local sampling method is inherently very limited and cannot in general identify the regions where the reconstruction has failed. In contrast, the proposed method can "globally" explore the latent space as long as the data likelihood is satisfied. Furthermore, $q(z|x)$ is only an approximate posterior distribution for a given $p(x|z)$ and $p(z)$ while we extract samples from the exact posterior. We compare the two methods also experimentally and show results for the local sampling in Section 4 as well.

2.3 Derivatives through the iterative matrix inversion

For the sampling procedure, we need to evaluate the terms in Eq. 3 at each iteration. This means the inverse of $(\Sigma_x^{-1} + E^H \Sigma_{ns}^{-1} E)$ has to be recomputed at each iteration, if the Σ_x term depends on the z value. In this work we take Σ_x to be constant, however, even then, inverting the matrix once and keeping it in memory is not an option, since it is a very big ($Nc \times Nc$) matrix. Approximating it as a diagonal matrix is also not an option as this would result in the loss of the aliasing information kept in the off-diagonals of the $E^H \Sigma_{ns}^{-1} E$ term.

Instead we propose to use an iterative matrix inversion that can also be applied when Σ_x changes with z . To this end, we write the common term in Eq. 3 in an approximation as

$$\gamma^* = \min_{\gamma} \|(\Sigma_x^{-1} + E^H \Sigma_{ns}^{-1} E)\gamma - \Sigma_x^{-1} \mu_x\|_2^2. \quad (4)$$

We then solve this inversion as an optimization problem using conjugate gradients (CG) and obtain γ^* , which we plug-in to Eq. 3 to yield

$$\log p(y|z) = \mu_x^H \Sigma_x^{-1} \gamma^* + 2\text{Re} \{ y^H \Sigma_{ns}^{-1} E \gamma^* \} - \frac{1}{2} \mu_x^H \Sigma_x^{-1} \mu_x, \quad (5)$$

where we dropped the constant C .

Though we use CG here, other gradient based methods can be used as well, since the gradients are well defined. Furthermore fast Fourier transform (FFT) can be used in the operations E and E^H , revoking the need to write the matrix explicitly and speeding up computations.

The key advantage here is that when the number of iterations (N_γ) for the CG is fixed, the whole inversion optimization also becomes a fixed operation, where the related vectors and matrices are added or multiplied with each other with fixed coefficients. Moreover, since automated differentiation is defined for all these operations separately, the gradient through the whole inversion operation can also

be taken using automated differentiation. This allows us to take the gradients of $p(y|z)$ according to z through this fixed optimization. Hence, before starting the Markov Chain we select the parameter N_γ for which we obtain a small L_2 error in Eq. 4 and keep this throughout the sampling. We observe that the error stays small throughout the sampling process for the chosen parameters for different μ_x values.

2.4 2D latent space VAE with an empirical prior

In the following we introduce the modified VAE model we use. Here we apply two modifications to the vanilla VAE model [14]. Firstly, the VAE is fully convolutional and we use a 2D latent space, i.e. $L_1 \times L_2 \times D$ dimensions with two spatial and one channel dimension, effectively a latent image with D channels. Each spatial position in such a latent image has a receptive field on the image when traced back and the architecture is designed using strided convolutions such that the receptive fields have only minimal overlap. This allows us to adhere to the independence assumption of the latent pixels reflected in the model by the use of a diagonal covariance matrix for $q(z|x)$. However, in reality, contents in receptive fields corresponding to different spatial locations in a latent image are not entirely independent from each other, as there are global correlations in the image. To be able to model these, we introduce an empirical prior as $p(z) = N(\mu_{pr}, \Sigma_{pr})$, similar to [21].

We obtain the parameters of $N(\mu_{pr}, \Sigma_{pr})$ empirically by sampling T samples $z_i \sim q(z|x_i)$ from T different training images x_i , after the VAE has been trained using a unit Gaussian prior. The mean μ_{pr} then is calculated as the mean of these samples. The estimation of a full covariance matrix is, however, difficult due to i) its size and ii) large number of samples required for the estimation. Instead we apply a Kolmogorov-Smirnov test [23] against the unit Gaussian separately for each latent channel to find the channels that are the least unit Gaussian in terms of the p-values, i.e. approximately the most informative. Then we form a combined block diagonal covariance matrix, where we calculate the full covariance matrix for the K most informative channels (of size $KL_1L_2 \times KL_1L_2$) and for the rest of the channels we assume they are independent from each other and calculate separately for each channel only the spatial covariance matrix (of size $L_1L_2 \times L_1L_2$). The proper combination of these block matrices yields the Σ_{pr} . In practice we do not form this matrix but implement the operations as sparse matrix-vector multiplications. This strategy also allows us to also re-

duce the number of samples T required for the estimation. We set $K = 10$ as preliminary experiments have shown this covers the informative channels sufficiently. We also set T high enough to make sure the estimated covariance matrix is full rank and found $T = 20000$ to be sufficient.

2.5 The extended encoding matrix

We extend the usual encoding operation in order to be able to model additional effects of the image acquisition. The aim while modeling these is to close the domain gap between a trained VAE and an observed k-space data by integrating acquisition specific knowledge as much as possible. Let us assume we have a trained VAE and observed a k-space data for the rest of this section.

The extended encoding matrix E is based on the usual MR encoding matrix $\tilde{E} = UFS$, with $S : \mathcal{C}^N \rightarrow \mathcal{C}^{Nc}$ the sensitivity encoding matrix [17] with c coils, $F : \mathcal{C}^{Nc} \rightarrow \mathcal{C}^{Nc}$ the coilwise Fourier transform, $U : \mathcal{C}^{Nc} \rightarrow \mathcal{C}^{Mc}$ the undersampling operation. Then the extended encoding operation is given as

$$E = \tilde{E}B\varphi Ps. \quad (6)$$

In the following we explain each term separately.

Firstly, a discrepancy between the k-space data and the space of images on which the VAE operates can be due to differences in the field of view (FOV). Though our fully convolutional architecture is agnostic to the image size, the empirical prior is estimated for a specific resolution and FOV, and the k-space size can be different due to varying FOV during acquisition. To bridge this gap, we introduce a padding operation P that pads or crops the images to fit the required sizes for the VAE.

Secondly, for computational as well as implementation related purposes, we assume that the phase of structural images are highly independent of the magnitude image and smooth, and hence a single phase image can be used for all posterior samples we take. This allows us to separate the magnitude and the phase of the image and run the sampling only on the magnitude of the image. However, note that this assumption is not a requirement for the proposed idea as the phase could be sampled as well, but rather a methodological simplification motivated by empirical observations. Following this assumption, we write the phase as a diagonal matrix φ acting on the image.

Thirdly, we use a diagonal matrix B that explicitly models the bias field in the acquisition [18]. The MR images unavoidably have a bias field due to several factors [19], and the bias field is difficult to avoid, however easy to estimate from the measured data. As

the bias varies between different acquisitions, this is a potential source of discrepancy leading to a domain shift. In order to minimize this, we train the VAE on bias free images, which then gives us bias free image samples. However, as the measured data y has the bias field in it, we estimate this field and explicitly model it to bring the sampled images to the biased domain of the k-space data.

Finally, we introduce a scale factor to make the data likelihood invariant to any scaling difference between the samples and the k-space. During the random walk in the latent space, the corresponding images might get scaled at each step, meaning the image may be multiplied globally by a scale factor. If this scale factor moves away from 1, this causes the data likelihood to increase, since the scales of the k-space data and the image samples do not match. However, from the perspective of sample quality, this does not pose a problem as long as the scaling factors are known. The sampled images can be brought to the same scale by multiplying them with the inverse of the scaling factor. Furthermore, allowing the scale factor to be different for each sample, allows more freedom to the random walk in the latent space, as it is less constrained by the increase in data likelihood due to scale changes. Hence such an invariance to this scaling is desirable. To this end we introduce a scalar s , that keeps the data likelihood at the lowest, inducing an invariance to scaling. We calculate its value by solving $s^* = \min_s \|Es\mu_x(z^t) - y\|_2^2$, where we separated only the s term from the extended encoding and used the mean of the decoder as the image. Then we take the derivative of the expression acc. to s and set it to zero to obtain the minimizing s value, which is given analytically as $s^* = \frac{Re\{\mu_x(z^t)^H E^H y\}}{\mu_x(z^t)^H E^H E \mu_x(z^t)}$. We do this estimation separately for each z^t sample at each step.

The complex conjugate of the extended encoding operation is given as $E^H = s^H P^H \varphi^H B^H \tilde{E}^H$, where we implement P^H as cropping if P is a padding operation and vice versa, φ^H is multiplication with the complex conjugate of the phase, $B^H = B$ since the bias field is real and $s^H = s$, again since the scale factor is real.

3 Experimental Setup

3.1 Data, training details and compared methods

We used T1 weighted slices from the full 3D volumes of 780 subjects from the HCP dataset [16] for training of the VAE. There were in total 202800 slices of

size 252x308, with an isotropic resolution of 0.7 mm. We ran the N4 bias field correction on the images and used the corrected images for training. The training ran for 2250000 iterations. We also trained another VAE after downsampling the images to 1mm isotropic resolution to work with lower resolution images for 1750000 iterations. For both, we augmented the images by translating them randomly (-4 to +4 pixels) in both directions and trained till convergence.

For testing we used 4 axial slices from subjects in the HCP dataset, different than those used in training, without bias field correction. We additionally tested with 3 axial slices from in-house measured T1 weighted brain images of different subjects [4]. These images have similar acquisition parameters as HCP and have an isotropic resolution of 1 mm. Furthermore these images are acquired with 13 coils and have non-zero phase. We used ESPIRiT [24] to obtain the coil sensitivity maps, which we used in the MAP estimation and sampling.

For the experiments, we retrospectively apply Cartesian undersampling to the test images with different patterns for each image. We obtain these patterns by generating 100 different patterns and choosing the one with the highest peak-to-side ratio of the associated point spread functions. In all patterns the 15 central profiles are always sampled.

For comparison purposes, we also modified the code by Adler et al. [9] to work with magnitude of MR images and evaluated in our experimental setting (the authors provided private access to their repository for the code). This method requires supervised training, i.e. pairs of zero-filled and fully sampled images. We generated such a training set with zero-filled images by undersampling the training images, which were also used for the VAE. We used the images with their bias field. We generated an undersampling pattern as described above, separately for each of the images. We trained the cWGAN for 800000 iterations till convergence with the the decay ratio for the noisy linear cosine decay as 2000000 but otherwise with the default settings in the code provided by the authors and the augmentation used for the VAE.

We also trained a feed-forward heteroscedastic network as a baseline. This network has the same architecture as the VAE, without the KLD in the loss and outputs a pixelwise standard deviation alongside the mean prediction. It is trained for 4000000 iterations using the supervised training setup described for the cWGAN method.

Finally, we implement the local sampling method we described in Section 2.2 for comparison purposes. For these we use the same VAE that is used in the proposed method. We take the samples around the

MAP reconstruction.

3.2 Implementation Details

We initialize the chain with the maximum-a-posteriori (MAP) images obtained by the deep density prior (DDP) reconstruction [4] to avoid a long burn-in period and take 10000 samples in total. We empirically determine the step size $\tau = 4 \times 10^{-4}$ to obtain an acceptance ratio around 0.3-0.5 and use the same for both the HCP images the in-house measured images. We take a lower number of samples (1000) for the cWGAN and local sampling methods as the effective sample size is also lower for the MCMC chain due to correlated samples.

We used Tensorflow [25] for the implementation of VAE related parts of the proposed method. The VAE is fully convolutional with all padded convolutions and has a 2 dimensional latent space with $D=60$ channels. We refer to the Appendix for the details of the architecture. For Σ_x we use a diagonal matrix with equal diagonal values set at 0.02. The same value was used for training of the VAE and sampling. Σ_{ns} was also taken to be a diagonal matrix, where the values were estimated by taking the variance of a small region at the upper 10 pixels of the fully sampled k-space center in the undersampled data, separately for each coil. Though this approach neglects the covariance between coils, it allows for a different variance per coil, which is important as these can differ significantly. Alternatively, the data can be pre-whitened to decorrelate the coils. The number of iterations for the matrix inversion were determined empirically as $N_\gamma = 25$, which was enough to reduce the L2 error of the approximate inversion below 0.01%.

For padding we use simple zero padding and cropping. For bias field estimation we used the N4 method [26] on the magnitude of the MAP estimation with default parameters. For the phase of the samples we took the MAP phase estimate.

4 Results

We show most of the results at high undersampling factors on purpose to make sure that the uncertainty in the inversion is high and demonstrate that the model is able to capture it. We present the results with the bias field put back in for convention although the method provides the samples bias free. We also multiply the images with their corresponding scale values to bring them to the same scale as the observed k-space data. The scale values stay mostly in the 0.95-1.1 range throughout the sampling procedure. We note that it is quite difficult to see the

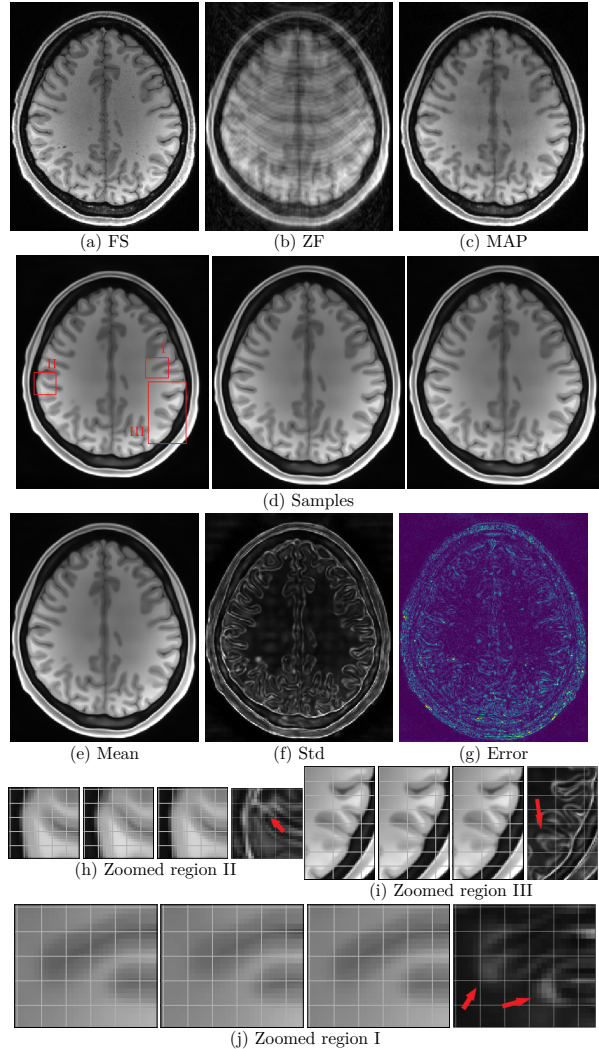


Figure 2: Results for the proposed latent MALA algorithm for $R=5$. FS, ZF and MAP denote the fully sampled, zero-filled and MAP estimation images. Second row presents three randomly chosen samples. (e-f) show the mean and pixelwise standard deviation (std) maps for all samples. (g) shows the absolute error map between the mean and the fully sampled image (clipped to 0-0.3). (h-j) show three zoomed-in regions indicated in (d) for three different samples as well as the pixelwise std maps. The grid lines are to aid visual inspection. As the variations are extremely difficult to see in this format, we strongly encourage the reader to look at the supplementary GIFs.

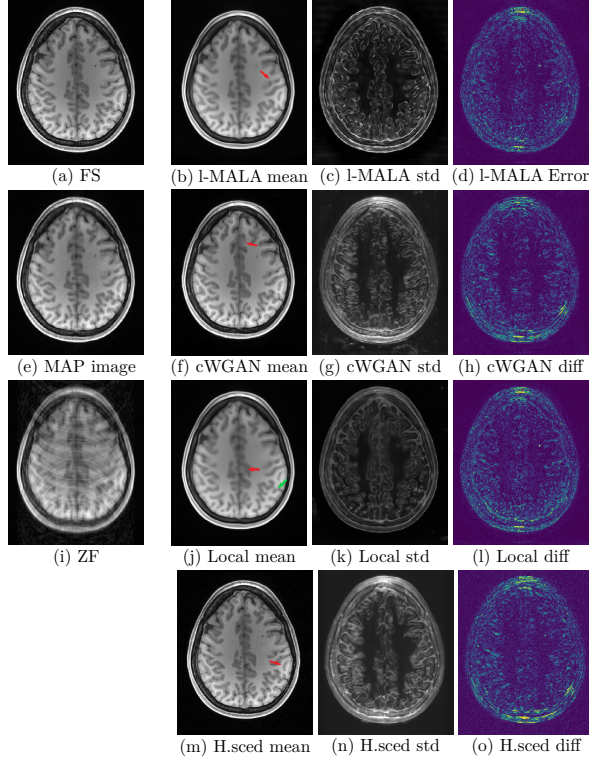


Figure 3: Sampling results for different methods at $R=5$. The left most column shows the fully sampled (FS), the MAP estimate and the zero-filled (ZF) images. In the rightmost three columns, the sample mean, pixelwise standard deviations and the absolute error maps between the mean and fully sampled images from the respective method are given. The error maps are clipped to $(0, 0.3)$, the std maps are clipped to $(0, 0.06)$ and $(0, 0.18)$ for the l-MALA and the other two methods, respectively.

variations in the samples presented in this paper in print and highly encourage the reader to view the provided GIFs¹.

We start by showing three sample images from the latent MALA model in Fig. 2 for an image undersampled with factor $R=5$. The structures in the samples as well as in the mean image, obtained as the mean of the drawn samples, overlap well with the fully sampled image. On the other hand, structural variations between the samples are present, which can also be seen in the std map. Nearly all pixels corresponding to tissue edges have a high std value. This is expected since the missing data in the k-space is mostly in the high-frequency regions, whose contributions are more important for edge pixels. However, it is important to

¹GIFs available for the shown results and additional images: <https://polybox.ethz.ch/index.php/s/3DPtRoYQnyzANAF>

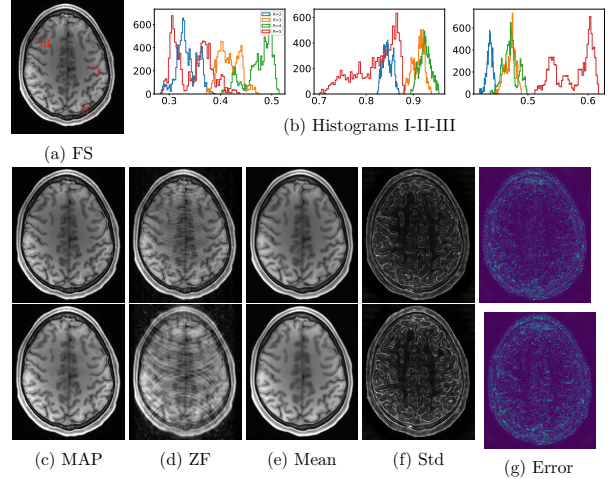


Figure 4: Results for changing undersampling ratios. First row shows the fully sampled image (FS) and histograms of pixels values in all samples for the pixels indicated on the FS image as I, II and III, respectively. Note the different bin positions for the histograms. Rows two and three show results for $R=2$ and $R=4$, respectively. Each row shows the MAP estimation, the zero filled image (ZF), the pixelwise mean and standard deviation maps and the absolute error map between the mean and the FS image (clipped to $(0,0.3)$).

note that the std values on the edges are not homogeneous, indicating some parts of the edges have higher variability. Furthermore, the variations are not limited to edges but also structures in the white matter as well. Examples of these can be seen in the zoomed regions, indicated with arrows. Region II shows an example where the grey matter is connected and disconnected in different samples. In the lower part of region III one can see a gray matter structure inside the white matter becoming more and less visible in the samples. Similarly, in region I, one can see a gray matter structure showing variability in how deep it penetrates the white matter. The pixel-wise std maps are marginal maps, i.e. they present the variations in the pixels as if they were independent. In reality the variations are not pixel-wise, rather the structures as collections of multiple pixels move between different samples, which can be observed better in the GIFs.

Fig. 3 shows results for the different sampling methods for comparison purposes, namely the latent MALA, the cWGAN and the local VAE sampling. We use the same undersampling pattern for all the methods for comparability. Both the VAE cWGAN methods capture the underlying image fairly well in

the mean of the samples, which is reflected in the difference images. The mean of the local VAE sampling is very blurry and cannot capture the structures in the underlying image as well as the other methods. The heteroscedastic model performs worse in the mean prediction as expected due to the lack of a data consistency term. The pixelwise standard deviation maps for the VAE and cWGAN models are similar at first glance, in that both reflect the high uncertainty regions at the tissue edges. However, the cWGAN maps are quite noisier and blurrier in comparison. Latent MALA provides a much finer level distinction. This is expected since the proposed method generates samples based on examination of the given data instead of relying on a trained model to generalize and does not make assumptions about data availability from the joint distribution of fully and undersampled images as in cWGAN. The std maps from the heteroscedastic model yields even more blurry results. All methods except the local sampling are capable of indicating some of the regions where their mean maps differ from the ground truth image, by showing high diversity in the samples or high std values in those regions, as exemplified by the arrows on the respective image. The local sampling method also captures variability on the edges. Furthermore, it can also indicate possible differences in its mean and the ground truth images, though only coincidentally. For example, in the region shown with the green arrow, it also assigns high std values, however this is rather due to the fact that there are two edges intersecting heavily in that region. In the region indicated by the red arrow, on the other hand, although the mean map differs from the ground truth, the local samples do not indicate a high variability in this region. We also present results in Appendix on how well the samples agree with the fully sampled image for the measured portion of the k-space and show that the l-MALA outperforms the local sampling and cWGAN methods in this regard.

In Fig. 4, we show how the statistics from the samples change with changing undersampling ratios. Firstly, we show histograms from three pixels indicated on the FS image for $R=2, 3, 4$ and 5 , from which one can observe that the pixel histograms become wider with increasing R , indicating higher uncertainty. This increase is also reflected in the std maps, which show an increase in std values for increasing R . This result shows that the proposed model is able to capture increasing ambiguity due to higher undersampling ratio.

Next we present results in Fig. 5 to show the methods sensitivity to the noise in the k-space. The quality of the MAP image degrades due to the high noise. This is reflected less in the mean maps, however the

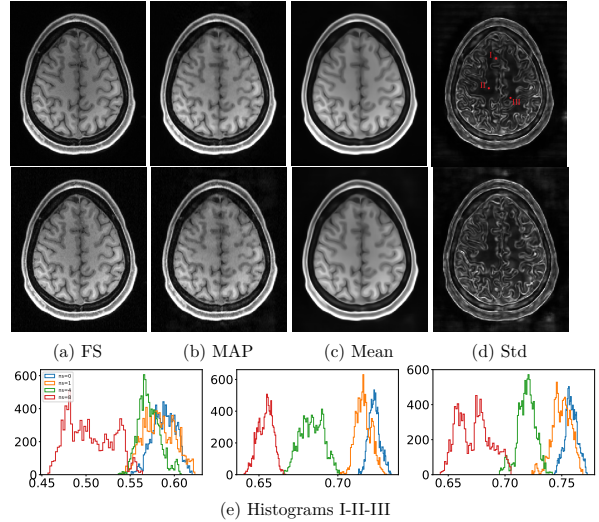


Figure 5: Results for changing the noise in k-space at $R=5$. First row shows the results with the basis HCP k-space noise. Second row shows the results with noise added on the k-space with 8 times the original noise standard deviation. Third row shows histograms of values of the pixels indicated on the std map (with added noise 1, 4 and 8 times of the basis noise). Note that the fully sampled (FS) image also changes due to the added noise.

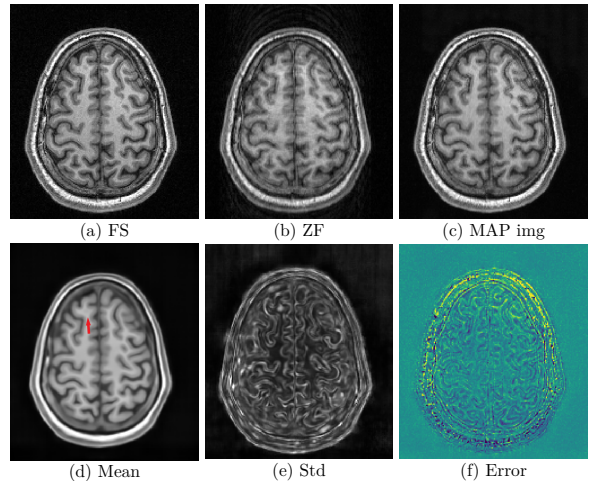


Figure 6: Results for multicoil in-house measured images at $R=2$. Shown are the fully sampled (FS), zero-filled (ZF), MAP estimate images, the mean and std maps for the latent-MALA samples as well as the difference image between the mean map and the FS (clipped to 0,0.3).

standard deviation values increase. This is how the model should behave since the added noise increases the values in Σ_{ns} , which then allows samples to move farther away from the measured data and show higher diversity. This is also reflected in the histograms of three pixel’s intensities, which are indicated in the top std map, as the distributions become wider with increasing noise.

Finally we present results for an image from the multicoil in-house measured dataset in Fig 6 for $R=2$. The method yields similar results for this image as well. The mean map can capture the underlying structures, and most variation is concentrated on the edges. Similar to the HCP results, std map can indicate potential discrepancies between mean and FS image as well, for instance low intensity region indicated with the arrow, that is incorrectly represented in the mean image, has a high std value.

5 Discussion

The results show that the proposed method is able to capture the underlying ambiguity in undersampled MRI acquisitions in that it generates samples, such as those in Fig. 2, that show realistic structural diversity while retaining high fidelity to the fully sampled image. The variability also indicates potential discrepancies between the mean prediction and the FS image.

One observation is that the texture in the fully sampled image is not entirely captured in the samples. This is firstly because we do not add the noise on to the samples, of which the texture is partly composed of. Secondly, the lack of texture can be attributed to the VAE, which is known for preferring blurry images and ignore very high-frequency changes. We expect this aspect to improve with a better prior model.

More importantly, the variation in the samples summarized in the std maps are capable of highlighting the potential mistakes in their mean predictions as seen in Fig. 3 for the latent MALA, cWGAN and heteroscedastic feed-forward network approaches. This is very valuable information for further decision making, as such regions where uncertainty is high should be approached with doubt. This information, when taken directly in the form of the samples or estimated standard deviations can be used for any decision making process for clinical or research purposes. The latent MALA and cWGAN are advantageous compared to heteroscedastic models in this respect as they can produce samples allowing quantification of uncertainty of any task per-

formed on the images. The heteroscedastic modeling approach is limited in that it makes an independent Gaussian assumption for each pixel and cannot generate realistic samples.

The std maps from the local VAE sampling do not highlight the regions where its mean differs from the ground truth. This is expected, since it takes the MAP estimate as the underlying image and samples only around its latent representation, without exploring other areas of the latent space. Hence it can generate variations only on the tissue edges of the MAP image, but cannot explore possibility of different tissue structures.

We note that the cWGAN method was developed for CT images and our modified implementation for MR is very straightforward and limited. By feeding only the magnitude images, we set the phase to zero, which is the correct phase for the HCP dataset, giving the method an advantage. However this is not a generic situation and the cWGAN method needs to be extended from CT to work in a realistic MR setting.

As the undersampling ratio R increases the inversion problem becomes harder, hence the mean maps start diverging more from the ground truth, which is also reflected in the difference maps shown in Fig. 4. Proposed model successfully captures the higher ambiguity for higher undersampling ratios as can be seen in the higher values in the std maps. This increase is also visible in the increasing spread of the histograms. Results presented in Fig. 5, from the experiments with increasing k-space noise Σ_{ns} , show that the latent MALA model can incorporate the changing k-space noise. When the k-space noise increases ambiguity in the observations increase. Mathematically, the Σ_{ns} term in the Gaussian data likelihood increases, which in turn allows accepting samples farther away from the measured k-space data y . This results in higher sample diversity, which is reflected in the increase in the standard deviation maps, whereas the mean of the samples is not affected much by this.

Though we use here the VAE as the latent space model, the outlined method is generic. The integral in Eq. 2, which relates the latent space and the k-space is a generic formulation and can be used with other probabilistic models that provide a deterministic or probabilistic decoder structure. One important necessary property, however, is that the decoder structure needs to be differentiable w.r.t. the latent variables for the Langevin walk. Utilizing another decoder structure here can also increase the quality of the final image samples, for instance models that suffer less from blurriness than VAEs.

Another factor to consider regarding the VAE is

that the aggregate posterior of the VAE, given as $q(z) = \int q(z|x)p_{data}(x)dx$ does not necessarily overlap with the prior distribution $p(z)$. This can then cause the random walk to move towards regions of the latent space which are not in the aggregate posterior or similarly miss parts of the aggregate posterior which are zero in the prior. We corrected this discrepancy partially by introducing the empirical prior for $p(z)$ and have not observed problems regarding this issue.

Similarly, MALA is not the only way of doing the sampling. We choose it due to several factors, such as its efficiency in high dimensional spaces, theoretical guarantees on asymptotic convergence to the true posterior, not requiring normalized target distributions etc. The target distribution $p(z|y)$ in our formulation is given by a Gaussian, however its covariance matrix is not given in a closed form, rendering direct sampling difficult. Furthermore, the Gaussian posterior is not a generic situation. In cases of more complicated distributions, approaches such as Hamiltonian Monte Carlo [11] can be utilized so that the typical set can be traversed more quickly. Similarly, in cases of multimodal distributions, approaches tailored to such distributions, such as Stein variational gradient descent [27] can be considered. Furthermore natural gradient based methods, where the geometry of the target distribution is taken into account by introducing an associated Riemannian metric can be considered to speed up the MALA [11].

As discussed above, the proposed method has the advantage of having a modular structure as the prior is decoupled from the data acquisition model and the target posterior is decoupled from the sampling procedure. This, we believe, is quite advantageous in terms of future research and improvement opportunities. This is in contrast to the cWGAN approach, where the loss function and the architecture, by design, determine an implicit target distribution without explicitly modeling the prior or the acquisition. Lastly, the decoupling of the prior from the data acquisition model allows the latent MALA model to be used for different undersampling factors with the same prior without retraining and also incorporate additional details of the acquisition in a very straightforward way, such as the bias field without needing to retrain the prior.

Lastly, the proposed model is sampling from the true posterior for a given $p(x)$ and y . Predictive approaches for uncertainty quantification, such as cWGAN, relies on a trained network to generalize for a given sample while having serious training data deficiency. They require training samples that show different fully sampled images for a given undersampled

image, which is not readily available unless a method such as the one proposed here is used to construct them.

6 Conclusion

In this paper we proposed and evaluated a method that can provide multiple possible images for the given undersampled k-space data. In contrast to reconstruction approaches, where a single image is output, the sampling approach can capture the uncertainty in the inversion process due to the missing data. The variation in the samples is indicative of the uncertainty, open up new avenues for uncertainty quantification for following image analysis tasks and can point to potential mistakes in the mean prediction. The method we propose has a modular structure and can be improved by separately improving its components, such as the prior term or the sampling scheme.

Acknowledgment

The authors thank GyroTools for their MRecon software, NVIDIA for their GPU donation and Klaas P. Pruessmann and Roger C. Luechinger for their help with data acquisition.

References

- [1] B. Bilgic, I. Chatnuntawech, A. P. Fan, K. Setsompop, S. F. Cauley, L. L. Wald, and E. Adalsteinsson, "Fast image reconstruction with l2-regularization," *Journal of Magnetic Resonance Imaging*, vol. 40, no. 1, pp. 181–191, 2014.
- [2] M. Lustig, D. Donoho, and J. M. Pauly, "Sparse MRI: The application of compressed sensing for rapid MR imaging," *Magnetic Resonance in Medicine*, vol. 58, no. 6, pp. 1182–1195, 2007.
- [3] J. Tsao, P. Boesiger, and K. P. Pruessmann, "k-t blast and k-t sense: Dynamic mri with high frame rate exploiting spatiotemporal correlations," *Magnetic Resonance in Medicine*, vol. 50, no. 5, pp. 1031–1042, 2003.
- [4] K. C. Tezcan, C. F. Baumgartner, R. Luechinger, K. P. Pruessmann, and E. Konukoglu, "Mr image reconstruction using deep density priors," *IEEE Transactions on Medical Imaging*, vol. 38, no. 7, 2019.

- [5] A. Kendall and Y. Gal, “What uncertainties do we need in bayesian deep learning for computer vision?” in *Advances in Neural Information Processing Systems 30*, 2017, pp. 5574–5584.
- [6] Y. Gal and Z. Ghahramani, “Bayesian convolutional neural networks with Bernoulli approximate variational inference,” *arXiv:1506.02158*, 2015.
- [7] R. Tanno, D. E. Worrall, A. G. Enrico Kaden, F. Grussu, A. Bizzi, S. N. Sotiropoulos, A. Criminisi, and D. C. Alexander, “Uncertainty quantification in deep learning for safer neuroimage enhancement,” *arXiv:1907.13418v1*, 2019.
- [8] J. Schlemper, D. C. Castro, W. Bai, C. Qin, O. Oktay, J. Duan, A. N. Price, J. Hajnal, and D. Rueckert, “Bayesian deep learning for accelerated mr image reconstruction,” in *Machine Learning for Medical Image Reconstruction*. Springer International Publishing, 2018.
- [9] J. Adler and O. Kten, “Deep bayesian inversion,” *arXiv:1811.05910*, 2018.
- [10] S. Pedemonte, C. Catana, and K. Van Leemput, “Bayesian tomographic reconstruction using riemannian mcmc,” in *Medical Image Computing and Computer-Assisted Intervention – MICCAI 2015*. Springer International Publishing, 2015, pp. 619–626.
- [11] M. Girolami and B. Calderhead, “Riemann manifold langevin and hamiltonian monte carlo methods,” *Journal of the Royal Statistical Society: Series B (Statistical Methodology)*, vol. 73, no. 2, 2011.
- [12] D. Narnhofer, K. Hammernik, F. Knoll, and T. Pock, “Inverse GANs for accelerated MRI reconstruction,” in *Wavelets and Sparsity XVIII*, D. V. D. Ville, M. Papadakis, and Y. M. Lu, Eds., vol. 11138, International Society for Optics and Photonics. SPIE, 2019, pp. 381 – 392.
- [13] J. Schlemper, J. Caballero, J. V. Hajnal, A. N. Price, and D. Rueckert, “A deep cascade of convolutional neural networks for dynamic mr image reconstruction,” *IEEE Transactions on Medical Imaging*, vol. 37, no. 2, pp. 491–503, 2018.
- [14] D. P. Kingma and M. Welling, “Auto-encoding variational bayes,” *CoRR*, vol. abs/1312.6114, 2013.
- [15] D. J. Rezende, S. Mohamed, and D. Wierstra, “Stochastic backpropagation and approximate inference in deep generative models,” in *Proceedings of the 31st International Conference on Machine Learning*, ser. Proceedings of Machine Learning Research, vol. 32, no. 2. Beijing, China: PMLR, 22–24 Jun 2014, pp. 1278–1286.
- [16] D. V. Essen, K. Ugurbil, E. Auerbach, D. Barch, T. Behrens, R. Bucholz, A. Chang, L. Chen, M. Corbetta, S. Curtiss, S. D. Penna, D. Feinberg, M. Glasser, N. Harel, A. Heath, L. Larson-Prior, D. Marcus, G. Michalareas, S. Moeller, R. Oostenveld, S. Petersen, F. Prior, B. Schlaggar, S. Smith, A. Snyder, J. Xu, and E. Yacoub, “The human connectome project: A data acquisition perspective,” *NeuroImage*, vol. 62, no. 4, pp. 2222 – 2231, 2012, connectivity.
- [17] K. P. Pruessmann, M. Weiger, P. Brnert, and P. Boesiger, “Advances in sensitivity encoding with arbitrary k-space trajectories,” *Magnetic Resonance in Medicine*, vol. 46, no. 4, pp. 638–651, 2001.
- [18] M. Gaillochet, K. Tezcan, and E. Konukoglu, “Joint reconstruction and bias field correction for undersampled mr imaging,” *MICCAI*, 2020.
- [19] P. G. Sled J.G., “Understanding intensity non-uniformity in mri,” *MICCAI*, 1998.
- [20] C. M. Bishop, *Pattern Recognition and Machine Learning (Information Science and Statistics)*. Berlin, Heidelberg: Springer-Verlag, 2006.
- [21] A. Volokitin, E. Erdil, N. Karani, K. C. Tezcan, X. Chen, L. V. Gool, and E. Konukoglu, “Modelling the distribution of 3d brain mri using a 2d slice vae,” *MICCAI*, 2020.
- [22] K. Tóthová, S. Parisot, M. C. H. Lee, E. Puyol-Antón, L. M. Koch, A. P. King, E. Konukoglu, and M. Pollefeys, “Uncertainty quantification in cnn-based surface prediction using shape priors,” in *Shape in Medical Imaging*. Springer International Publishing, 2018, pp. 300–310.
- [23] W. W. Daniel, *Applied Nonparametric Statistics*. Duxbury, 2000.
- [24] U. Martin, L. Peng, M. M. J., V. Patrick, E. Michael, P. J. M., V. S. S., and L. Michael, “Espiritan eigenvalue approach to autocalibrating parallel mri: Where sense meets grappa,” *Magnetic Resonance in Medicine*, vol. 71, no. 3, pp. 990–1001, 2014.

- [25] M. Abadi, P. Barham, J. Chen, Z. Chen, A. Davis, J. Dean, M. Devin, S. Ghemawat, G. Irving, M. Isard, M. Kudlur, J. Levenberg, R. Monga, S. Moore, D. G. Murray, B. Steiner, P. Tucker, V. Vasudevan, P. Warden, M. Wicke, Y. Yu, and X. Zheng, “Tensorflow: A system for large-scale machine learning,” in *12th USENIX Symposium on Operating Systems Design and Implementation (OSDI 16)*, 2016, pp. 265–283.
- [26] N. J. Tustison, B. B. Avants, P. A. Cook, Y. Zheng, A. Egan, P. A. Yushkevich, and G. J. C., “N4itk: Improved n3 bias correction.” *IEEE Transactions on Medical Imaging*, vol. 29, 2010.
- [27] Q. Liu and D. Wang, “Stein variational gradient descent: A general purpose bayesian inference algorithm,” 2016.

A Appendix to “Sampling possible reconstructions of undersampled acquisitions in MR imaging”

A.1 Derivation of the closed form of $p(y|z)$

As mentioned in the paper the form that is easiest to interpret is given by the marginalization, however this integral difficult to evaluate directly. Instead, we do it implicitly by using conjugacy relations for Normal distributions.

We begin by writing

$$p(y|x, z)p(x|z) = p(y|z)p(x|y, z). \quad (7)$$

Since $p(y|x, z)$ and $p(x|z)$ are Normal distributions, due to the conjugacy, the posterior $p(x|y, z)$ is also a Normal distribution given as $N(\mu_{post}, \Sigma_{post})$. Then

$$p(y|z) = \frac{p(y|x, z)p(x|z)}{N(\mu_{post}, \Sigma_{post})}, \quad \text{or} \quad p(y|z)N(\mu_{post}, \Sigma_{post}) = p(y|x, z)p(x|z). \quad (8)$$

Hence the posterior $p(y|z)$ acts as a normalizer to the product distribution to yield a Gaussian. We derive $p(y|z)$ using this relation in Eqn. 8. In the following we also use the conditional independence $p(y|x, z) = p(y|x)$ meaning that when the image is given, this posterior distribution in the k-space is determined without the need for the latent variable.

For the derivation we use this strategy: i) we first write the product of the two distributions $p(y|x)p(x|z)$, ii) then recognize the mean and covariance of the Normal posterior distribution $N(\mu_{post}, \Sigma_{post})$ in this, iii) and separate a the Gaussian with these parameters from the whole expression. What is left gives us the target distribution.

The product can be written as

$$p(y|x)p(x|z) = \quad (9)$$

$$\det(2\pi\Sigma_{ns})^{-1/2} \det(2\pi\Sigma_x)^{-1/2} \exp \left\{ -\frac{1}{2} [(y - Ex)^H \Sigma_{ns}^{-1} (y - Ex)] \right\} \quad (10)$$

$$\cdot \exp \left\{ -\frac{1}{2} [(x - \mu_x)^H \Sigma_x^{-1} (x - \mu_x)] \right\} \quad (11)$$

$$= \det(2\pi\Sigma_{ns})^{-1/2} \det(2\pi\Sigma_x)^{-1/2} \exp \left\{ -\frac{1}{2} x^H \underbrace{(\Sigma_x^{-1} + E^H \Sigma_{ns}^{-1} E)}_{\Sigma_{post}^{-1}} x \right\} \quad (12)$$

$$+ Re\{x^H \underbrace{(E^H \Sigma_{ns}^{-1} y + \Sigma_x^{-1} \mu_x)}_{\Sigma_{post}^{-1} \mu_{post}}\} - \frac{1}{2} y^H \Sigma_{ns}^{-1} y - \frac{1}{2} \mu_x^H \Sigma_x^{-1} \mu_x \}, \quad (13)$$

where we have recognized the parameters of the posterior. With these we have enough information to complete the posterior Gaussian. We can replace the terms with posterior parameters and add the missing term $\pm \frac{1}{2} \mu_{post}^H \Sigma_{post}^{-1} \mu_{post}$ to complete the quadratic form as well as the normalizing determinant $\det(2\pi\Sigma_{post})^{\pm 1/2}$.

$$= \det(2\pi\Sigma_{ns})^{-1/2} \det(2\pi\Sigma_x)^{-1/2} \det(2\pi\Sigma_{post})^{+1/2} \det(2\pi\Sigma_{post})^{-1/2} \quad (14)$$

$$\cdot \exp \left\{ \underbrace{-\frac{1}{2} x^H \Sigma_{post}^{-1} x + Re\{x^H \Sigma_{post}^{-1} \mu_{post}\} - \frac{1}{2} \mu_{post}^H \Sigma_{post}^{-1} \mu_{post}}_{-\frac{1}{2} (x - \mu_{post})^H \Sigma_{post}^{-1} (x - \mu_{post})} \right\} \quad (15)$$

$$+ \frac{1}{2} \mu_{post}^H \Sigma_{post}^{-1} \mu_{post} - \frac{1}{2} y^H \Sigma_{ns}^{-1} y - \frac{1}{2} \mu_x^H \Sigma_x^{-1} \mu_x \}. \quad (16)$$

We can combine the quadratic term in the exponent with the determinant term and obtain the complete

posterior Gaussian. In this case the expression becomes

$$p(y|x)p(x|z) = N(\mu_{post}, \Sigma_{post}) \det(2\pi\Sigma_{ns})^{-1/2} \det(2\pi\Sigma_x)^{-1/2} \det(2\pi\Sigma_{post})^{+1/2} \quad (17)$$

$$\cdot \exp \left\{ + \frac{1}{2} \mu_{post}^H \Sigma_{post}^{-1} \mu_{post} - \frac{1}{2} y^H \Sigma_{ns}^{-1} y - \frac{1}{2} \mu_x^H \Sigma_x^{-1} \mu_x \right\}. \quad (18)$$

Remembering Eqn. 8, we obtain

$$p(y|z) = \frac{\det(2\pi\Sigma_{post})^{+1/2}}{\det(2\pi\Sigma_{ns})^{1/2} \det(2\pi\Sigma_x)^{1/2}} \cdot \exp \left\{ - \frac{1}{2} y^H \Sigma_{ns}^{-1} y + \frac{1}{2} \mu_{post}^H \Sigma_{post}^{-1} \mu_{post} - \frac{1}{2} \mu_x^H \Sigma_x^{-1} \mu_x \right\}. \quad (19)$$

Now taking the logarithm and leaving out the terms that are independent of z we can arrive at the expression we use as

$$\log p(y|z) = + \frac{1}{2} \mu_{post}^H \Sigma_{post}^{-1} \mu_{post} - \frac{1}{2} \mu_x^H \Sigma_x^{-1} \mu_x + C, \quad (20)$$

where C denotes some constant with z. Notice that we could leave out the determinant term in the nominator due to our model choice of constant Σ_x .

Now we need the closed form expression for the first term in the above equation. Also we need to arrive at this using the terms we have access to from the above equations 12 and 13, namely $\Sigma_{post}^{-1} \mu_{post}$ and Σ_{post}^{-1} . First we write $\mu_{post} = (\Sigma_{post}^{-1})^{-1} \Sigma_{post}^{-1} \mu_{post}$ and rewrite the target term as $\mu_{post}^H \Sigma_{post}^{-1} \mu_{post} = (\Sigma_{post}^{-1} \mu_{post})^H \mu_{post}$. Combining the expressions and isolating the terms constant with z as C then yields

$$\mu_{post}^H \Sigma_{post}^{-1} \mu_{post} = \mu_x^H \Sigma_x^{-1} (\Sigma_x^{-1} + E^H \Sigma_{ns}^{-1} E)^{-1} \Sigma_x^{-1} \mu_x \quad (21)$$

$$+ 2\text{Re} \{ y^H \Sigma_{ns}^{-1} E (\Sigma_x^{-1} + E^H \Sigma_{ns}^{-1} E)^{-1} \Sigma_x^{-1} \mu_x \} + C \quad (22)$$

Applying the Woodbury identity on the term $(\Sigma_x^{-1} + E^H \Sigma_{ns}^{-1} E)$ followed by some algebraic manipulations reveals that this is equivalent to the expression given in [22].

A.2 The VAE architecture

All convolutions are padded and have a kernel size (3, 3) and stride (1, 1) and use a ReLU unless noted otherwise.

The encoder begins with four convolutional layers with 32, 64, 64, 64 output channels, respectively. Then a convolutional layer with kernel size (14, 14), stride (19, 19) and 60 output channels produces the mean of $q(z|x)$ from the fourth layer. Similarly another convolutional layer from the third layer produces the log standard deviation values for $q(z|x)$ with a kernel size of (14, 14), stride (19, 19), without ReLU and 60 output channels. The network is fully convolutional, hence can work with different image sizes. Assuming an input image size of 252x308 for demonstration, the latent space size becomes bx18x22x60, where b is the batch size. We use the usual reparameterization trick to sample z's [14]. At the beginning of the decoder, we apply a scheme of increasing channel dimensions and using these to increase spatial dimensions. We do this in two steps, once for the first image dimension and once again for the second image dimension to obtain a proper reshaping while using the implementation of Tensorflow's reshaping function. First convolutional layer of the decoder does not use ReLU and has 64·19=1216 output channels, resulting in a tensor of size bx18x22x1216. The output of this layer is first transposed to bx18x1216x22 and reshaped to bx252x64x22. This layer then gets transposed to bx252x22x64, then goes through a convolutional layer with again 1216 output channels and without ReLU and becomes bx252x22x1216. This then gets reshaped again to yield a tensor size of bx252x308x64, which is the input image size. This tensor then goes through a ReLU. We then apply 6 convolutional layers with each 60 output channels. Finally another convolutional layer with 1 output channel yields the mean prediction.

A.3 Distribution of voxelwise error in the measured parts of k-space and RMSE

Here we show the k-space error histograms in Figure 7 for a test slice at R=5. We calculate these as follows: we take 50 image samples $\{x_s\}_{s=1}^{50}$ from each method and apply the undersampled Fourier transform to transform each of them to k-space and take the measured voxels. Then we calculate the voxelwise difference

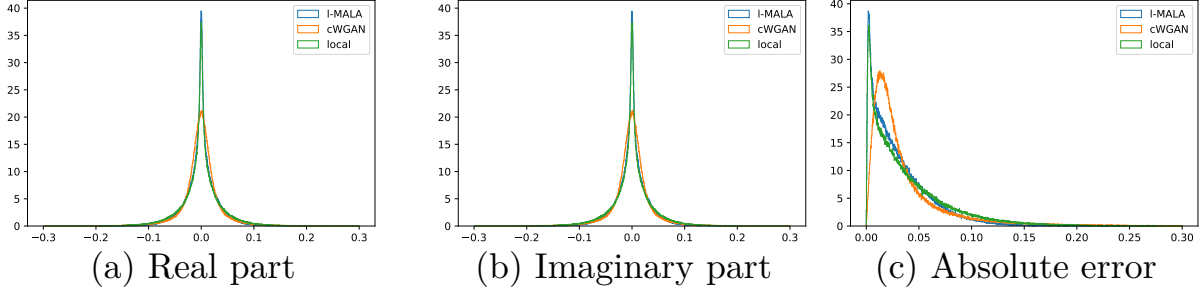


Figure 7: Histograms of the voxelwise error in the measured voxels in the k-space for three different methods for a subject at R=5. As the error is complex, the real and imaginary parts as well as the magnitude of the error values are shown separately.

between these and the measured data for all measured k-space voxels for all the samples together. The histogram then shows the distribution of the error for all these k-space voxels from all 50 samples. As this difference is complex, we show two histograms separately for the real and imaginary parts and also for the magnitude values. We can also look at the image-wise the absolute error as

$$\text{abs. error}_s = \sum_{\text{all meas. voxels}} |Ex_{FS} - Ex_s|, \quad (23)$$

for a sample image x_s , the fully sampled image x_{FS} and the sum is over all measured k-space voxels. When calculated for all 50 samples, the mean (std) values for this slice are given as 484.23 (5.45), 584.71 (18.89) and 597.98 (15.69), for the l-MALA, cWGAN and local sampling methods, respectively.

To show how this generalizes, we do a similar analysis using slices from 9 test subjects. We undersample the slices with different undersampling patterns at R=5. Again, for each test subject we generate 50 samples for the three methods each. We then calculate the absolute errors and report the mean (std) values in Table 1. For all subjects (except subject 3) the l-MALA method yields significantly (p value lower than 0.001) lower absolute error for the 50 samples with the Wilcoxon signed-rank test. For subject 3, the cWGAN method yields significantly lower absolute error (p value lower than 0.001). Considering the mean absolute error for each subject, the l-MALA method yields significantly lower absolute error overall (p value lower than 0.011). We also calculate the root mean squared error (RMSE) between the 50 samples and the fully sampled image. Though achieving a low RMSE is not the purpose of any of the methods, we present these results as they still provide some insight into the performance of the methods. To calculate the RMSE we use the formula given in [4] and use a mask to disregard the background. The RMSE values are significantly lower for the 50 samples for each subject (p value lower than 0.001) and for the mean RMSE values for each subject (p value lower than 0.008) for the l-MALA method compared to the other methods.

subject	Abs. error			RMSE		
	l-MALA	cWGAN	Local	l-MALA	cWGAN	Local
#1	639.55 (6.67)	679.18 (20.68)	808.54 (11.14)	9.29 (0.12)	11.29 (0.32)	11.67 (0.14)
#2	651.38 (7.02)	711.14 (22.23)	765.40 (7.42)	11.22 (0.10)	13.43 (0.44)	12.86 (0.12)
#3	518.36 (2.32)	497.98 (18.08)	570.67 (6.10)	13.18 (0.07)	15.51 (0.77)	14.51 (0.16)
#4	573.19 (3.24)	614.66 (18.35)	699.97 (7.15)	8.91 (0.08)	11.00 (0.57)	10.86 (0.13)
#5	482.08 (2.83)	584.71 (18.89)	597.98 (15.69)	8.50 (0.08)	11.38 (0.57)	10.34 (0.13)
#6	603.95 (5.45)	647.72 (16.12)	775.51 (11.20)	8.16 (0.05)	9.85 (0.37)	10.21 (0.13)
#7	595.17 (9.36)	694.03 (22.71)	754.85 (8.49)	9.08 (0.14)	12.48 (0.52)	11.01 (0.11)
#8	623.54 (7.65)	717.40 (19.04)	752.28 (7.06)	10.14 (0.19)	12.79 (0.41)	12.07 (0.09)
#9	528.14 (6.39)	556.63 (12.26)	646.52 (7.50)	8.11 (0.07)	10.11 (0.39)	9.70 (0.092)

Table 1: Absolute error and RMSE values for 9 test subjects at R=5.